

# Non-Hermitian Floquet second order topological insulators in periodically quenched lattices

Jiaxin Pan<sup>1</sup> and Longwen Zhou<sup>1,\*</sup>

<sup>1</sup>*Department of Physics, College of Information Science and Engineering, Ocean University of China, Qingdao 266100, China*

(Dated: 2025-03-26)

Higher-order topological phases are characterized by protected states localized at the corners or hinges of the system. By applying time-periodic quenches to a two-dimensional lattice with balanced gain and loss, we obtain a rich variety of non-Hermitian Floquet second order topological insulating phases. Each of the phases is characterized by a pair of integer topological invariants, which predict the numbers of Floquet corner modes at zero and  $\pi$  quasienergies. We establish the topological phase diagram of the model, and find a series of non-Hermiticity induced transitions between different Floquet second order topological phases. We further generalize the mean chiral displacement to two-dimensional non-Hermitian systems, and use it to extract the topological invariants of our model dynamically. This work thus extend the study of higher-order topological matter to more generic nonequilibrium settings, in which the interplay between Floquet engineering and non-Hermiticity yields fascinating new phases.

## I. INTRODUCTION

Higher-order topological phases (HOTPs) have attracted great attention in recent years [1–7]. They are featured by localized states appearing at the boundaries of their boundaries. More precisely, an HOP of order  $n$  in spatial dimension  $d$  ( $\geq n$ ) possesses topologically protected gapless states at its  $(d-n)$ -dimensional boundaries. Over the years, a rich variety of HOTPs have been found in insulating [8–27], superconducting [28–42] and semi-metallic [43–48] systems, and further classified according to their protecting symmetries [49–51]. Experimentally, HOTPs have also been realized in solid-state [52–56], photonic [57–63], acoustic [64–71] systems and electrical circuits [72–75], triggering the interest over a wide range of research areas.

Recently, the study of HOTPs have been extended to nonequilibrium settings, in which time-periodic driving fields or gains and losses are applied to a given static system, leading to the discovery of Floquet HOTPs [76–86] and non-Hermitian HOTPs [87–94]. The Floquet HOTPs are distinguished from their static cousins by their unique space-time symmetries, topological invariants, and anomalous Floquet corner or hinge states. On the other hand, the HOTPs in non-Hermitian systems are featured by non-Bloch topological invariants, hybrid higher-order skin modes and biorthogonal bulk-boundary correspondence. Yet, under more general conditions, a static system could subject to both time-dependent driving fields and non-Hermitian effects, and much less is known about the fate of HOTPs in such driven open systems. Moreover, the collaboration of drivings and dissipation may induce exotic non-Hermitian Floquet HOTPs that are absent in either closed Floquet systems or non-driven non-Hermitian systems, which certainly deserve

careful investigations.

In this work, based on the coupled-wire construction of HOTPs [76], we introduce a class of second order topological insulator (SOTI) model by coupling an array of one-dimensional (1D) topological insulators along a second spatial dimension with dimerized hoppings. Under time-periodic quenches and balanced onsite gains and losses, we find rich non-Hermitian Floquet SOTI phases in our system, which are protected by the sublattice symmetry. We introduce a pair of integer topological invariants to characterize the found topological phases, and establish the topological phase diagram of our model. A series of topological phase transitions and non-Hermitian Floquet SOTI phases with large topological invariants are found by varying the amplitude of driving fields or the strength of gains and losses. Under the open boundary conditions (OBCs), many non-Hermitian Floquet zero and  $\pi$  modes emerge at the corners of the system, whose numbers are predicted by the bulk topological invariants. Finally, we propose a way to dynamically extract the topological invariants of our system by measuring the mean chiral displacements of a wave packet.

## II. MODEL AND SYMMETRY

In this section, we first introduce an SOTI model following the coupled-wire construction of static and Floquet SOTIs [76]. Our non-Hermitian Floquet SOTI system is then realized by applying time-periodic quenches and balanced onsite gains and losses to the static SOTI model.

We start with a prototypical tight-binding Hamiltonian  $H$ , which describes particles hopping on a two-

\* zhoulw13@u.nus.edu

dimensional (2D) square lattice,

$$\begin{aligned} H = & \sum_{i,j} [J + (-1)^i \delta] (|i, j\rangle\langle i+1, j| + \text{H.c.}) \\ & + \sum_{i,j} J_1 (|i, 2j\rangle\langle i, 2j+1| + \text{H.c.}) \\ & + \sum_{i,j} (-1)^j (i J_2 |i, j\rangle\langle i, j+2| - \mu |i, j\rangle\langle i, j| + \text{H.c.}). \end{aligned} \quad (1)$$

Here  $i$  ( $j$ ) denotes the lattice site index along the  $x$  ( $y$ ) direction of the system. Along the  $x$ -direction,  $J - \delta$  ( $J + \delta$ ) corresponds to the intracell (intercell) hopping amplitude. Along the  $y$ -direction,  $J_1$  and  $J_2$  characterize the nearest- and next-nearest-neighbor hopping amplitudes, and  $\mu$  denotes the strength of a staggered onsite potential. The system described by  $H$  can thus be viewed as an array of tight-binding wires lying along the  $y$ -direction, with each of them being connected to its adjacent wires by Su-Schrieffer-Heeger (SSH)-type dimerized couplings [95]. Such kind of “coupled-wire construction” has been demonstrated to be a powerful way of engineering both static and Floquet SOTIs [76] in closed systems. Generally speaking, zero-energy topological corner modes would appear in the system if both the SSH-type couplings along  $x$ -direction and the wires along  $y$ -direction are set in topologically nontrivial regimes.

Taking periodic boundary conditions (PBCs) along both  $x, y$  directions and performing Fourier transformations, we can express  $H$  in the momentum representation as  $H = \sum_{k_x, k_y} |k_x, k_y\rangle H(k_x, k_y)\langle k_x, k_y|$ , where the Hamiltonian matrix  $H(k_x, k_y)$  has a Kronecker sum structure

$$H(k_x, k_y) = H_x(k_x) \otimes \tau_0 + \sigma_0 \otimes H_y(k_y), \quad (2)$$

with

$$H_x(k_x) = [(J - \delta) + (J + \delta) \cos k_x] \sigma_x + (J + \delta) \sin k_x \sigma_y, \quad (3)$$

$$H_y(k_y) = 2J_1 \cos k_y \tau_x + 2(\mu + J_2 \sin k_y) \tau_z. \quad (4)$$

Here  $k_x, k_y \in [-\pi, \pi]$  are the quasimomenta along  $x$  and  $y$  directions.  $\sigma_0$  and  $\tau_0$  are both  $2 \times 2$  identity matrices, with  $\mathbb{I}_4 \equiv \sigma_0 \otimes \tau_0$ .  $\sigma_{x,y,z}$  and  $\tau_{x,y,z}$  are Pauli matrices acting in the sublattice spaces in the  $x$  and  $y$  directions, respectively. It is well known that both  $H_x(k_x)$  and  $H_y(k_y)$  describe 1D topological insulators, which are characterized by integer winding numbers. When the conditions  $|J - \delta| < |J + \delta|$  and  $|\mu| < |J_2|$  are satisfied, the 1D descendant systems  $H_x(k_x)$  and  $H_y(k_y)$  are both in topologically nontrivial phases at half-filling. In this case, according to the analysis in Ref. [76], the parent Hamiltonian  $H$  describes an SOTI with four corner modes under the OBCs.

In this work, we investigate whether the interplay between time-periodic drivings and dissipation effects could induce exotic non-Hermitian Floquet SOTI phases

with multiple topological corner modes in the system described by  $H$ . To do so, we introduce balanced gain and loss to the staggered onsite potential  $\mu$ , i.e., by setting  $\mu = u + iv$  with  $u, v \in \mathbb{R}$ . Furthermore, we apply piecewise time-periodic quenches to each of the wires along the  $y$ -direction, so that  $H_y(k_y)$  becomes

$$H_y(k_y, t) = 2J_1 \cos k_y f_1(t) \tau_x + 2(\mu + J_2 \sin k_y) f_2(t) \tau_z, \quad (5)$$

where the quench protocols are described by

$$f_1(t) \equiv \sum_{\ell \in \mathbb{Z}} \left[ \theta \left( \ell + \frac{1}{2} - \frac{t}{T} \right) - \theta \left( \ell - \frac{t}{T} \right) \right], \quad (6)$$

$$f_2(t) \equiv \sum_{\ell \in \mathbb{Z}} \left[ \theta \left( \ell + 1 - \frac{t}{T} \right) - \theta \left( \ell + \frac{1}{2} - \frac{t}{T} \right) \right], \quad (7)$$

with  $\theta(t)$  and  $T$  being the step function and driving period. The Floquet operator of the system, which generates its time evolution over a complete driving period  $T$ , is then given by  $U = \sum_{k_x, k_y} |k_x, k_y\rangle U(k_x, k_y)\langle k_x, k_y|$ , with

$$U(k_x, k_y) = e^{-iH_x(k_x)} \otimes e^{-i(\mu + J_2 \sin k_y) \tau_z} e^{-iJ_1 \cos k_y \tau_x}. \quad (8)$$

where we have set the unit of energy to be  $\hbar/T$  and with  $\hbar = T = 1$ . Without loss of generality, we choose to work with the topological flat-band limit of  $H_x(k_x)$ , which can be achieved by setting  $J = \delta = \Delta/2$  [95]. With these considerations, the Floquet operator of our system now simplifies to

$$U(k_x, k_y) = e^{-iH_0(k_x)} \otimes e^{-ih_z(k_y) \tau_z} e^{-ih_x(k_y) \tau_x}, \quad (9)$$

where

$$H_0(k_x) = \Delta(\cos k_x \sigma_x + \sin k_x \sigma_y), \quad (10)$$

$$h_x(k_y) = J_1 \cos k_y, \quad (11)$$

$$h_z(k_y) = u + iv + J_2 \sin k_y. \quad (12)$$

Note that  $U(k_x, k_y)$  is nonunitary due to the balanced gain and loss  $\pm iv$  in the staggered onsite potential  $\mu \tau_z$ .

Before characterizing the topological properties of our non-Hermitian Floquet system, we first analyze the symmetries that allow it to possess corner modes at zero and  $\pi$  quasienergies under the OBCs. Following the established approach to the symmetry analysis of Floquet operators [96, 97], we first transform  $U(k_x, k_y)$  in Eq. (9) to a pair of symmetric time frames upon similarity transformations, yielding

$$U_\alpha(k_x, k_y) = \mathcal{U}_0(k_x) \otimes \mathcal{U}_\alpha(k_y). \quad (13)$$

Here  $\alpha = 1, 2$  and

$$\mathcal{U}_0(k_x) = e^{-iH_0(k_x)}, \quad (14)$$

$$\mathcal{U}_1(k_y) = e^{-i\frac{h_x(k_y)}{2}\tau_x} e^{-ih_z(k_y)\tau_z} e^{-i\frac{h_x(k_y)}{2}\tau_x}, \quad (15)$$

$$\mathcal{U}_2(k_y) = e^{-i\frac{h_z(k_y)}{2}\tau_z} e^{-ih_x(k_y)\tau_x} e^{-i\frac{h_z(k_y)}{2}\tau_z}. \quad (16)$$

It is clear that  $U(k_x, k_y)$ ,  $U_1(k_x, k_y)$  and  $U_2(k_x, k_y)$  are similar to one another, and therefore sharing the same complex Floquet quasienergy spectrum. Furthermore, both  $U_1(k_x, k_y)$  and  $U_2(k_x, k_y)$  possess the sublattice symmetry  $\mathcal{S} = \sigma_z \otimes \tau_y$ , i.e.,

$$SU_\alpha(k_x, k_y)\mathcal{S} = U_\alpha^{-1}(k_x, k_y) \quad (17)$$

for  $\alpha = 1, 2$ , with  $\mathcal{S} = \mathcal{S}^\dagger$  and  $\mathcal{S}^2 = \mathbb{I}_4$ . Besides, we can also identify the diagonal ( $\mathcal{M}_+$ ) and off-diagonal ( $\mathcal{M}_-$ ) spatial symmetries of  $U_\alpha$  as

$$\mathcal{M}_\pm U_\alpha(k_x = \pm k_y) \mathcal{M}_\pm^{-1} = U_\alpha^{-1}(k_x = \pm k_y). \quad (18)$$

The spatial symmetries  $\mathcal{M}_\pm$  (which are simply equal to  $\mathcal{S}$  here) guarantee the zero- and  $\pi$ -quasienergy Floquet modes, if presence, should appear at the four corners of the system under the OBCs, whereas the degeneracy of these non-Hermitian Floquet corner modes are protected by the sublattice symmetry  $\mathcal{S}$ .

### III. TOPOLOGICAL INVARIANTS

With the relevant symmetries in hand, we will now introduce the topological invariants of our system.

According to the topological classification of Floquet operators [96, 97], a Floquet system in one-dimension is characterized by integer winding numbers. This has been demonstrated for both Hermitian [98–101] and non-Hermitian [102–105] Floquet models. Since the Floquet operator  $U(k_x, k_y)$  of our system in Eq. (9) has a Kronecker product structure, its topological invariants may be constructed from the winding numbers of descendant 1D models  $\mathcal{U}_0(k_x)$  and  $\mathcal{U}_\alpha(k_y)$  ( $\alpha = 1, 2$ ) in the symmetric time frames. To do so, we first note that  $\mathcal{U}_0(k_x)$  is simply the evolution operator of a static SSH model over a period. Its topological winding number  $w$  is therefore equal to 1 (0) in the topologically nontrivial (trivial) regime [95]. For the parameter choice in Eq. (10), we simply have  $w = 1$ . Furthermore, applying the Euler formula to Eqs. (15) and (16), the Floquet operator  $\mathcal{U}_\alpha(k_y)$  ( $\alpha = 1, 2$ ) can be expanded as

$$\mathcal{U}_\alpha(k_y) = \cos[\mathcal{E}(k_y)] - i[d_{\alpha x}(k_y)\tau_x + d_{\alpha z}(k_y)\tau_z]. \quad (19)$$

Here the complex quasienergy dispersion is

$$\mathcal{E}(k_y) = \arccos\{\cos[h_x(k_y)]\cos[h_z(k_y)]\}, \quad (20)$$

and the components of complex-valued vectors

$[d_{\alpha x}(k_y), d_{\alpha z}(k_y)]$  for  $\alpha = 1, 2$  are given by

$$d_{1x}(k_y) = \sin[h_x(k_y)]\cos[h_z(k_y)], \quad (21)$$

$$d_{1z}(k_y) = \sin[h_z(k_y)], \quad (22)$$

$$d_{2x}(k_y) = \sin[h_x(k_y)], \quad (23)$$

$$d_{2z}(k_y) = \cos[h_x(k_y)]\sin[h_z(k_y)]. \quad (24)$$

The number of times that the two-component vector  $[d_{\alpha x}(k_y), d_{\alpha z}(k_y)]$  winds around zero when  $k_y$  sweeps across the first Brillouin zone defines the topological winding number of  $\mathcal{U}_\alpha(k_y)$  [102–105] for  $\alpha = 1, 2$ , i.e.,

$$w_\alpha = \int_{-\pi}^{\pi} \frac{dk_y}{2\pi} \frac{d_{\alpha x}\partial_{k_y}d_{\alpha z} - d_{\alpha z}\partial_{k_y}d_{\alpha x}}{d_{\alpha x}^2 + d_{\alpha z}^2}. \quad (25)$$

Note in passing that even though  $d_{\alpha x}(k_y)$  and  $d_{\alpha z}(k_y)$  can take complex values, their imaginary parts would have no contributions to  $w_\alpha$  as shown in Ref. [105].

Using the winding numbers  $w$  and  $w_\alpha$  defined separately for  $\mathcal{U}_0(k_x)$  and  $\mathcal{U}_\alpha(k_y)$  ( $\alpha = 1, 2$ ) in Eq. (13), we can construct the topological invariants of the 2D Floquet operator  $U_\alpha(k_x, k_y)$  in the  $\alpha$ 's time frame as

$$\nu_\alpha = w w_\alpha, \quad \alpha = 1, 2. \quad (26)$$

Finally, by combining  $\nu_1$  and  $\nu_2$ , we obtain a pair of integer topological invariants  $(\nu_0, \nu_\pi)$ , given by

$$\nu_0 = \frac{\nu_1 + \nu_2}{2}, \quad \nu_\pi = \frac{\nu_1 - \nu_2}{2}. \quad (27)$$

It tends out that the invariants  $(\nu_0, \nu_\pi)$  could fully characterize the non-Hermitian Floquet SOTI phases of  $U(k_x, k_y)$  in Eq. (8). Moreover, we well demonstrate that under the OBCs, these topological invariants correctly predict the numbers of non-Hermitian Floquet corner modes at zero and  $\pi$  quasienergies. In the Hermitian limit, the invariants  $(\nu_0, \nu_\pi)$  could also characterize the SOTI phases of the resulting closed Floquet system [76], so long as the corresponding Floquet operator  $U(k_x, k_y)$  shares the tensor product structure with Eq. (8).

### IV. TOPOLOGICAL PHASE DIAGRAM

In this section, based on the topological invariants introduced in Eq. (27), we present the topological phase diagram of our non-Hermitian Floquet SOTI model.

From Eqs. (25) and (26), it is clear that  $\nu_0 \neq 0$  ( $\nu_\pi \neq 0$ ) in Eq. (27) if both  $w$  and  $\frac{\nu_1 + \nu_2}{2}$  ( $\frac{\nu_1 - \nu_2}{2}$ ) are nonzero. As the parameters of the 1D descendant system in the  $x$ -direction in Eq. (10) has been set inside the topological nontrivial regime, we have the winding number  $w = 1$  for  $\mathcal{U}_0(k_x)$ . A topological phase transition in our system is then accompanied by the closing and reopening of a point gap of  $\mathcal{U}_\alpha(k_y)$  at the quasienergy zero or  $\pi$  on the complex plane.

According to Eq. (20), the gapless condition of  $\mathcal{U}_\alpha(k_y)$

is determined by

$$\cos[\mathcal{E}(k_y)] = \cos[h_x(k_y)] \cos[h_z(k_y)] = \pm 1, \quad (28)$$

where the  $+1$  ( $-1$ ) on the right hand side of Eq. (28) corresponds to a point-gap closing at  $\mathcal{E}(k_y) = 0$  [ $\mathcal{E}(k_y) = \pi$ ]. With the help of Eqs. (11) and (12), Eq. (28) is equivalent to the following two equalities

$$\sin(u + J_2 \sin k_y) = 0, \quad (29)$$

$$\cos(J_1 \cos k_y) \cos(u + J_2 \sin k_y) \cosh v = \pm 1. \quad (30)$$

Combining these equations, we can express the gapless condition of  $\mathcal{U}_\alpha(k_y)$  in Eq. (13) as

$$v = \pm \text{arccosh} \left\{ \frac{1}{\cos \left[ J_1 \sqrt{1 - (n\pi - u)^2 / J_2^2} \right]} \right\}, \quad (31)$$

where  $n \in \mathbb{Z}$  and  $|n\pi - u| < |J_2|$ . Eq. (31) determines the boundaries between different topological phases in the parameter space, across which the system described by  $U(k_x, k_y)$  in Eq. (9) is expected to change from one non-Hermitian Floquet SOTI phase to another.

In the following, we present the topological phase diagrams of our periodically quenched non-Hermitian lattice model (8) in two typical situations. In the first case, we show the phase diagram versus the real and imaginary parts of the onsite potential  $\mu = u + iv$  in Fig. 1. The other system parameters are chosen as  $J = \delta = \Delta/2 = \pi/40$ ,  $J_1 = 0.5\pi$  and  $J_2 = 5\pi$ . The values of topological invariants  $(\nu_0, \nu_\pi)$ , obtained from Eqs. (25)-(27), are shown explicitly in Fig. 1 within each of the non-Hermitian Floquet SOTI phases. The black lines separating different phases (regions with different colors) in Fig. 1 are obtained from the gapless condition Eq. (31). From the phase diagram, we observe a series of topological phase transitions accompanied by quantized jumps of  $\nu_0$  and/or  $\nu_\pi$  by varying either the real or imaginary part of  $\mu$ . Therefore, the existence of balanced onsite gains and losses can indeed induce phase transitions and new types of non-Hermitian Floquet SOTIs in our system. Furthermore, we found a couple of SOTI phases characterized by large topological invariants  $(\nu_0, \nu_\pi)$ . Detailed numerical calculations suggest that the values of  $(\nu_0, \nu_\pi)$  can be arbitrarily large with the increase of the hopping amplitude  $J_2$ . These SOTI phases originate from the interplay between the time-periodic driving fields  $f_{1,2}(t)$  and the onsite gains and losses, and are thus unique to non-Hermitian Floquet systems. Under the OBCs, a non-Hermitian Floquet SOTI phase with large invariants  $(\nu_0, \nu_\pi)$  will also admit multiple quartets of topological corner modes at zero and  $\pi$  quasienergies, as will be demonstrated in the next section.

In the second case, we present the topological phase diagram of our model versus the hopping amplitude  $J_1$  and the imaginary part of onsite potential  $v$  in Fig. 2. The other system parameters are fixed at  $J = \delta = \Delta/2 =$

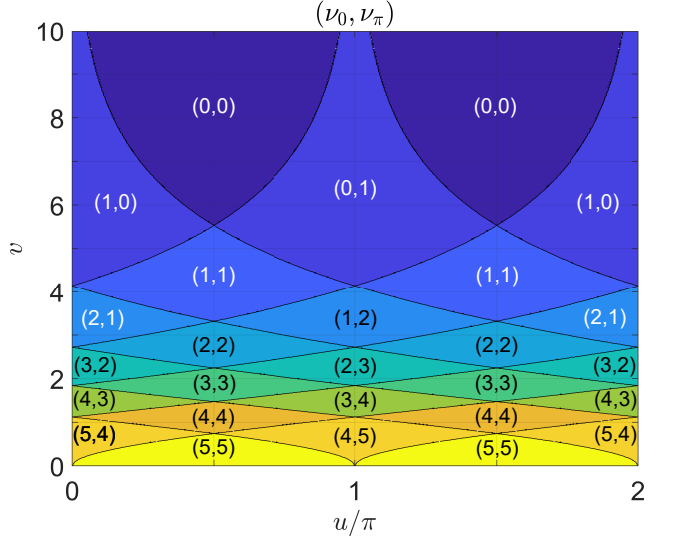


FIG. 1. Topological phase diagram of the periodically quenched non-Hermitian lattice model (9) versus the real and imaginary parts of onsite potential  $\mu = u + iv$ . The other system parameters are fixed at  $\Delta = \pi/20$ ,  $J_1 = 0.5\pi$  and  $J_2 = 5\pi$ . Each region with a uniform color corresponds to a non-Hermitian Floquet SOTI phase, whose topological invariants  $(\nu_0, \nu_\pi)$  are denoted explicitly therein. The black lines separating different phases are determined by the gapless condition Eq. (31).

$\pi/40$ ,  $u = 0$ , and  $J_2 = 3\pi$ . The values of topological invariants  $\nu_0$  and  $\nu_\pi$  for each of the phases are shown separately in the panels (a) and (b) of Fig. 2, respectively. Similar to the first case, we observe rich non-Hermitian Floquet SOTI phases and phase transitions at different values of  $J_1$  and  $v$ . Moreover, around certain values of  $J_1$  (e.g.,  $J_1 = 2.5\pi$ ), we find that by increasing the gain and loss strength  $v$ , the system can shift to topological phases with larger invariants, which could also support more quartets of corner modes under the OBCs. Such kinds of non-Hermiticity *enhanced* topological properties are usually unexpected in systems with losses. Therefore, it forms one of the defining features of our construction, with potential applications in combating environmental effects in quantum information tasks.

To summarize, we find rich non-Hermitian Floquet SOTI phases with large topological invariants in our system. In the following two sections, we discuss two experimentally relevant signatures of the intriguing phases found here. We first present the Floquet spectrum and corner modes of our system under the OBCs, and establish correspondence between these corner modes and the bulk topological invariants  $(\nu_0, \nu_\pi)$ . Next, we show how to extract the invariants  $(\nu_0, \nu_\pi)$  from the nonunitary stroboscopic dynamics of easily prepared wave packets.

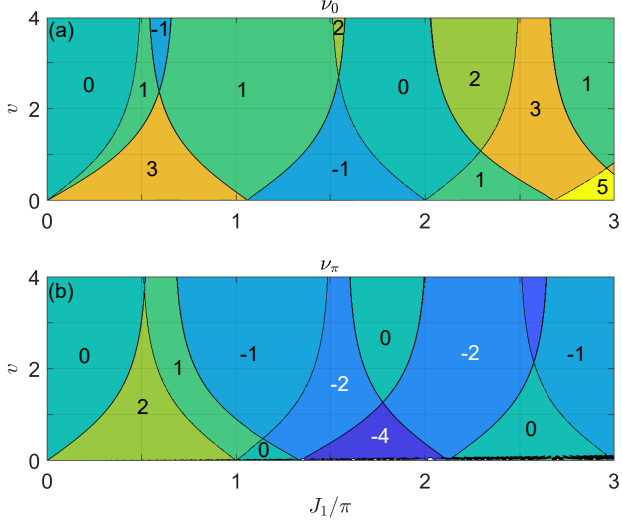


FIG. 2. Topological phase diagram of the periodically quenched non-Hermitian lattice model (9) versus the hopping amplitude  $J_1$  and gain or loss amplitude  $v$ . The other system parameters are  $\Delta = \pi/20$ ,  $J_2 = 3\pi$  and  $u = 0$ . The values of topological invariants  $\nu_0$  ( $\nu_\pi$ ) for each non-Hermitian Floquet SOTI phase with a uniform color are shown in panel (a) [(b)]. The black lines separating different phases are obtained from the gapless condition Eq. (31).

## V. CORNER STATES AND BULK-CORNER CORRESPONDENCE

Under the OBCs, the Floquet operator of our periodically quenched lattice model (8) takes the form

$$U = U_x \otimes U_y, \quad (32)$$

where

$$U_x = e^{-i \sum_{i,j} \frac{\Delta[1+(-1)^j]}{2} (|i,j\rangle\langle i+1,j| + \text{H.c.})}, \quad (33)$$

$$U_y = e^{-i \sum_{i,j} (-1)^j (iJ_2|i,j\rangle\langle i,j+2| - \mu|i,j\rangle\langle i,j| + \text{H.c.})} \times e^{-i \sum_{i,j} J_1 (|i,2j\rangle\langle i,2j+1| + \text{H.c.})}. \quad (34)$$

The number of lattice sites along the  $x$  ( $y$ ) direction is  $L_x = 2N_x$  ( $L_y = 2N_y$ ), with  $N_x$  ( $N_y$ ) being the number of unit cells. The Floquet quasienergy spectrum and corner modes of the model can be obtained by solving the eigenvalue equation  $U|\Psi\rangle = e^{-iE}|\Psi\rangle$ , where  $E$  is the quasienergy and  $|\Psi\rangle$  is the corresponding Floquet eigenstate. Note that due to the balanced gain and loss in the onsite potential  $\mu = u + iv$ , the quasienergy  $E$  is in general a complex number. We define a quasienergy gap in this case as a point on the complex plane, which is avoided by all the bulk eigenstates for a given set of system parameters.

In the topological nontrivial regime, a 2D SOTI is featured by topologically protected zero energy modes around the corners of the lattice. In a non-Hermitian Floquet SOTI, there could be two types of topological corner

modes, whose quasienergies are zero and  $\pi$ . For the class of periodically quenched lattice model studied in this work, the physical origin of these corner modes can be directly inferred from the Kronecker product structure of Floquet operator  $U$  in Eq. (32). That is, if the 1D descendant systems  $U_x$  and  $U_y$  both possess zero quasienergy edge modes, they will couple to form a Floquet corner mode with quasienergy zero in the parent 2D system described by  $U$  in Eq. (32). Similarly, if the 1D system  $U_x$  ( $U_y$ ) possesses a zero ( $\pi$ ) quasienergy edge mode, they will couple to form a Floquet corner mode with quasienergy  $\pi$  in the parent system  $U = U_x \otimes U_y$ . These corner modes are robust to perturbations that break the tensor product structure of  $U$ , so long as the sublattice symmetry  $\mathcal{S}$  is preserved. Moreover, the above analyses indicate that the number of non-Hermitian Floquet corner modes with quasienergy zero ( $\pi$ ) in the 2D system is  $n_0 = n_{x0}n_{y0}$  ( $n_\pi = n_{x0}n_{y\pi}$ ), where  $n_{x0}$  is the number of zero edge modes of  $U_x$  and  $n_{y0}$  ( $n_{y\pi}$ ) is the number of zero ( $\pi$ ) edge modes of  $U_y$ . Combining these observations with the invariants  $(\nu_0, \nu_\pi)$  defined in Eq. (27), we could build the connection between numbers of non-Hermitian Floquet corner modes  $(n_0, n_\pi)$  and the bulk topological numbers as

$$n_0 = 4|\nu_0|, \quad n_\pi = 4|\nu_\pi|. \quad (35)$$

Eq. (35) establishes the bulk-corner correspondence of 2D Floquet systems with the structure of Eq. (32), which also holds in the Hermitian limit ( $\mu \in \mathbb{R}$ ) so long as the sublattice symmetry  $\mathcal{S}$  is retained. Note in passing that the system described by  $U_x$  in Eq. (33) is essentially static, and therefore could only possess edge modes at zero quasienergies.

To demonstrate the topological phase transitions and bulk-corner correspondence of our system, we present the Floquet spectrum of  $U$  in Eq. (32) under the OBCs for two typical examples. In order to show the evolution of spectral gaps with the system parameters in a more transparent manner, we introduce a pair of spectral (point) gap functions, defined as

$$G_0 = \frac{1}{\pi} \sqrt{(\text{Re}E)^2 + (\text{Im}E)^2}, \quad (36)$$

$$G_\pi = \frac{1}{\pi} \sqrt{(|\text{Re}E| - \pi)^2 + (\text{Im}E)^2}. \quad (37)$$

It is clear that when the system becomes gapless at the quasienergy  $E = 0$  ( $E = \pm\pi$ ), we will have  $G_0 = 0$  ( $G_\pi = 0$ ). In Fig. 3(a), we show the evolutions of  $G_0$  (red circles) and  $G_\pi$  (blue lines) versus the real part  $u$  of the onsite potential. The other system parameters are chosen as  $\Delta = \pi/20$ ,  $J_1 = 0.5\pi$ ,  $J_2 = 5\pi$  and  $v = 0.5$ . The number of non-Hermitian Floquet zero and  $\pi$  corner modes ( $n_0, n_\pi$ ) are denoted explicitly at  $G_0 = G_\pi = 0$ , and the ticks  $(u_1, u_2)$  along the horizontal axis are determined by the gapless condition Eq. (31). We see that across each topological phase transition point  $u_i$  ( $i = 1, 2$ ), the number of Floquet corner modes  $n_0$  or  $n_\pi$  changes by

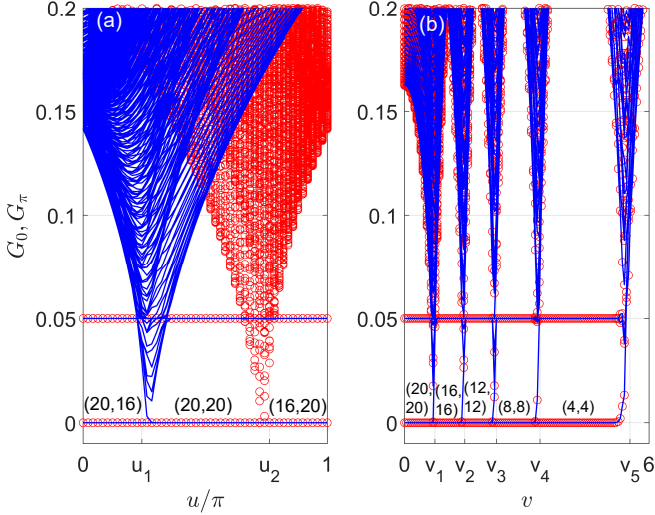


FIG. 3. Spectral gap functions  $G_0$  (red circles) and  $G_\pi$  (blue lines) versus the real and imaginary parts of onsite potential  $\mu = u + iv$ . The system parameters are  $\Delta = \pi/20$ ,  $J_1 = 0.5\pi$ ,  $J_2 = 5\pi$  and  $v = 0.5$  ( $u = 0.5\pi$ ) for panel (a) [(b)]. The numbers of non-Hermitian Floquet topological corner modes at zero (with  $G_0 = 0$ ) and  $\pi$  (with  $G_\pi = 0$ ) quasienergies ( $n_0, n_\pi$ ) are denoted explicitly in each panel. The ticks  $u_i$  ( $i = 1, 2$ ) and  $v_i$  ( $i = 1, 2, 3, 4, 5$ ) along the horizontal axis are the bulk phase transition points deduced from Eq. (31).

an integer multiple of four. Within the three topological phases separated by  $u_1$  and  $u_2$ , the numbers of corner modes ( $n_0, n_\pi$ ) are related to the topological invariants ( $\nu_0, \nu_\pi$ ) in Fig. 1 by Eq. (35), which confirms the bulk-corner correspondence in our system. In Fig. 3(b), we show the changes of  $G_0$  (red circles) and  $G_\pi$  (blue lines) versus the imaginary part  $v$  of the onsite potential, with the other system parameters being set as  $\Delta = \pi/20$ ,  $J_1 = 0.5\pi$ ,  $J_2 = 5\pi$  and  $u = 0.5\pi$ . Similarly, we observe that the numbers of corner modes ( $n_0, n_\pi$ ) are related to the topological invariants ( $\nu_0, \nu_\pi$ ) by Eq. (35). Moreover, the values of ( $n_0, n_\pi$ ) change by four across every transition point  $v_i$  ( $i = 1, 2, 3, 4, 5$ ) along the horizontal axis. We thus conclude that a series of transitions between different non-Hermitian Floquet SOTI phases can indeed be induced by simply varying the magnitude of gain and loss  $v$ , and SOTI phases unique to non-Hermitian Floquet systems could emerge after each transition in our model.

To further unveil the potential of non-Hermitian effects in generating Floquet SOTI phases with more corner modes, we present the spectral gap functions ( $G_0, G_\pi$ ) in red circles and blue dots versus the gain and loss amplitude  $v$  in Fig. 4(a). The other system parameters are fixed at  $\Delta = \pi/20$ ,  $J_1 = 2.5\pi$ ,  $J_2 = 3\pi$  and  $u = 0$ . It is clear that with the increase of  $v$ , the numbers of corner modes ( $n_0, n_\pi$ ) changes from (4, 0) to (12, 0) across  $v_1$  and from (12, 0) to (12, 8) across  $v_2$ , consisting with the bulk-corner relation Eq. (35). Such an *enhancement* of topological signatures in deeper non-Hermitian regimes

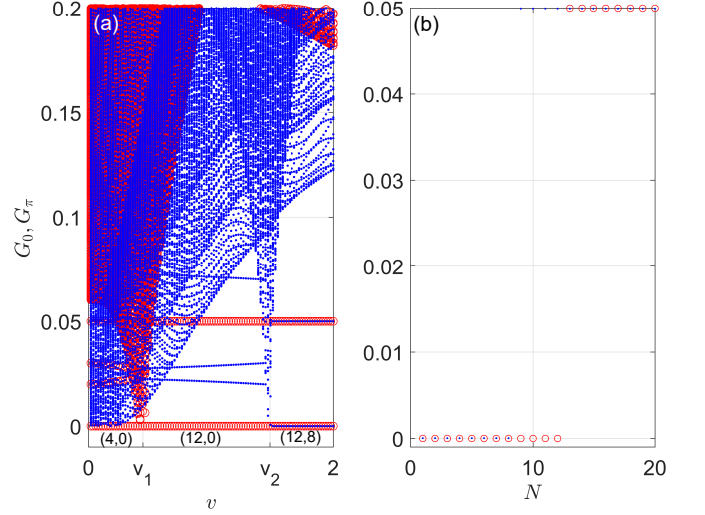


FIG. 4. Spectral gap functions  $G_0$  (red circles) and  $G_\pi$  (blue dots) versus the imaginary part  $v$  of the onsite potential in panel (a) and the state index  $N$  in panel (b). The system parameters are set as  $\Delta = \pi/20$ ,  $J_1 = 2.5\pi$ ,  $J_2 = 3\pi$  and  $u = 0$  in panel (a), with further  $v = 2$  in panel (b).  $v_1$  and  $v_2$  refer to the topological phase transition points obtained from Eq. (31), and the numbers of non-Hermitian Floquet zero and  $\pi$  corner modes ( $n_0, n_\pi$ ) for each topological phases are denoted explicitly in panel (a).

is intriguing, which might be used to design new topological state preparation schemes and achieve quantum information tasks in open systems. To see the numbers and profiles of the Floquet corner modes more explicitly, we show the first twenty states of the system at  $v = 2$  in Fig. 4(b), with the other system parameters chosen to be the same as in Fig. 4(a). The twelve (eight) non-Hermitian Floquet corner modes at the quasienergy zero ( $\pi$ ) are denoted by red circles (blue dots), whose probability distributions are shown in Figs. 5(a)-(c) [Figs. 5(d)-(e)]. We see that these modes are indeed well-localized around the four corners of the 2D lattice, which are protected by the sublattice symmetry  $\mathcal{S} = \sigma_z \otimes \tau_y$  introduced in Sec. II.

## VI. DYNAMICAL CHARACTERIZATION OF THE TOPOLOGICAL PHASES

The mean chiral displacement (MCD) is first introduced as the time-averaged chiral displacement  $\hat{x}\mathcal{S}$  of an initially localized wave packet in a 1D lattice within the symmetry classes AIII and BDI [106]. Later, it is generalized to Floquet systems [99, 107], non-Hermitian systems [103, 104], interacting systems [108], systems in other symmetry classes [101] and higher physical dimensions [76]. Experimentally, the MCD has been measured in cold atom [109] and photonic [110] setups. In this section, we extend the definition of MCD to 2D non-Hermitian Floquet systems with sublattice symmetry,

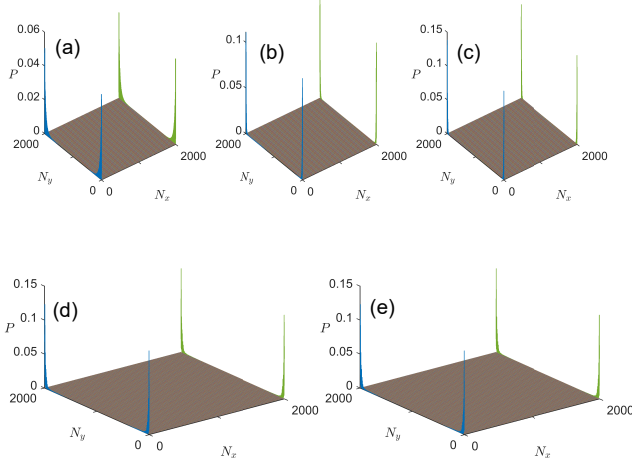


FIG. 5. Probability distributions  $P$  of the non-Hermitian Floquet topological corner modes at quasienergies zero [in panels (a), (b), (c)] and  $\pi$  [in panels (d), (e)]. The lattice contains  $N_x = N_y = 2000$  unit cells along  $x$  and  $y$  directions. The system parameters are the same as those of Fig. 4(b), yielding twelve zero corner modes and eight  $\pi$  corner modes under the OBCs.

and demonstrate how to extract the topological invariants of our model dynamically from the MCDs.

For a 2D lattice model with the the sublattice symmetry  $\mathcal{S}$ , we define its chiral displacement operator as  $\mathcal{C} = \hat{r} \otimes \mathcal{S}$ , with  $\hat{r}$  being the unit cell position operator. The chiral displacement of a wave packet  $\rho_0$  in the symmetric time frame  $\alpha$  is then given by

$$C_\alpha(t) = \text{Tr} \left( \rho_0 \tilde{U}_\alpha^{\dagger t} \mathcal{C} U_\alpha^t \right), \quad (38)$$

where  $\alpha = 1, 2$ ,  $t$  counts the number of driving periods, and the trace  $\text{Tr}(\dots)$  is taken over all degrees of freedom of the system. To build the connection between  $C_\alpha$  and the topological invariants  $(\nu_0, \nu_\pi)$  of the system in a most straightforward manner, we prepare the initial state  $\rho_0$  in the central unit cell  $(m, n) = (0, 0)$  of the lattice, with all the four sublattices being uniformly filled, i.e.,  $\rho_0 = |0, 0\rangle\langle 0, 0| \otimes \mathbb{I}_4/4$ . For our periodically quenched lattice model Eq. (9),  $U_\alpha$  is given by the inverse Fourier transform of Eq. (13), and  $\tilde{U}_\alpha$  is defined such that if  $|\Psi\rangle$  is a right eigenvector of  $U_\alpha$  with eigenvalue  $e^{-iE}$ , it is the left eigenvector of  $\tilde{U}_\alpha$  with the same eigenvalue.

In the following, we will relate the long-time average of  $C_\alpha(t)$  to the topological invariants of 2D non-Hermitian Floquet operators with the structure of Eq. (13) and the sublattice symmetry  $\mathcal{S}$ . Note that in the Hermitian limit, we simply have  $\tilde{U}_\alpha = U_\alpha$ , and our derivations below will also hold. Taking the trace in Eq. (38) explicitly and inserting the identities in the lattice and momentum rep-

resentations, we find

$$C_\alpha(t) = \frac{1}{4} \sum_{k_x, k_y, k'_x, k'_y} \sum_{mn} mn \langle 0, 0 | k_x, k_y \rangle \langle k_x, k_y | m, n \rangle \\ \times \langle m, n | k'_x, k'_y \rangle \langle k'_x, k'_y | 0, 0 \rangle \text{tr} \left[ \tilde{U}_\alpha^{\dagger t}(k_x, k_y) \mathcal{S} U_\alpha^t(k'_x, k'_y) \right], \quad (39)$$

where the trace  $\text{tr}[\dots]$  in the second line is only taken over the sublattice degrees of freedom. Using the Fourier expansion  $|m, n\rangle = \frac{1}{\sqrt{N_x N_y}} \sum_{k_x, k_y} e^{i(k_x m + k_y n)} |k_x, k_y\rangle$ , Eq. (39) can be simplified to

$$C_\alpha(t) = \frac{1}{4} \sum_{k_x, k'_x} \sum_{k_y, k'_y} \sum_{mn} \frac{mn}{N_x^2 N_y^2} e^{i(k_x m + k_y n)} \\ \times e^{-i(k'_x m + k'_y n)} \text{tr} \left[ \tilde{U}_\alpha^{\dagger t}(k_x, k_y) \mathcal{S} U_\alpha^t(k'_x, k'_y) \right]. \quad (40)$$

With the help of summation formulas  $\sum_m m e^{i(k_x - k'_x)m} = iN_x \partial_{k'_x} \delta_{k_x k'_x}$  and  $\sum_n n e^{i(k_y - k'_y)n} = iN_y \partial_{k'_y} \delta_{k_y k'_y}$ , we further obtain

$$C_\alpha(t) = \frac{1}{4} \sum_{k_x, k'_x} \sum_{k_y, k'_y} \frac{1}{N_x N_y} (i\partial_{k'_x} \delta_{k_x k'_x}) \\ \times (i\partial_{k'_y} \delta_{k_y k'_y}) \text{tr} \left[ \tilde{U}_\alpha^{\dagger t}(k_x, k_y) \mathcal{S} U_\alpha^t(k'_x, k'_y) \right]. \quad (41)$$

Finally, taking the continuous limit  $N_j \rightarrow \infty$ , we have  $N_j \delta_{k_j k'_j} \rightarrow \delta(k_j - k'_j)$  and  $\sum_{k_j, k'_j} \rightarrow N_j^2 \int_{-\pi}^{\pi} \frac{dk_j}{2\pi} \int_{-\pi}^{\pi} \frac{dk'_j}{2\pi}$  for  $j = x, y$ . Eq. (41) then becomes

$$C_\alpha(t) = \int_{-\pi}^{\pi} \frac{dk_x}{2\pi} \int_{-\pi}^{\pi} \frac{dk_y}{2\pi} \\ \times \frac{1}{4} \text{tr} \left[ \tilde{U}_\alpha^{\dagger t}(k_x, k_y) \mathcal{S} (i\partial_{k_x} i\partial_{k_y}) U_\alpha^t(k_x, k_y) \right]. \quad (42)$$

For our periodically quenched lattice model, the expression of chiral displacement  $C_\alpha(t)$  can be further simplified. Noting the tensor product structure of Floquet operator  $U_\alpha$  in Eq. (13) and the expression of sublattice symmetry operator  $\mathcal{S} = \sigma_z \otimes \tau_y$ , we can write  $C_\alpha(t)$  as a product of chiral displacements in the descendant 1D systems as  $C_\alpha(t) = C_x(t) C_{\alpha y}(t)$  [111], where

$$C_x(t) = \int_{-\pi}^{\pi} \frac{dk_x}{2\pi} \frac{1}{2} \text{tr} \left[ \mathcal{U}_0^{\dagger t}(k_x) \sigma_z i\partial_{k_x} \mathcal{U}_0^t(k_x) \right], \quad (43)$$

$$C_{\alpha y}(t) = \int_{-\pi}^{\pi} \frac{dk_y}{2\pi} \frac{1}{2} \text{tr} \left[ \tilde{\mathcal{U}}_\alpha^{\dagger t}(k_y) \tau_y i\partial_{k_y} \mathcal{U}_\alpha^t(k_y) \right]. \quad (44)$$

Summing up the chiral displacements over different numbers  $t$  of the driving period and taking the long-time average, we obtain the MCD of our system in the  $\alpha$ 's time

frame as

$$\begin{aligned} \bar{C}_\alpha &= \lim_{t \rightarrow \infty} \frac{1}{t} \sum_{t'=1}^t C_x(t') \quad (45) \\ &\times \int_{-\pi}^{\pi} \frac{dk_y}{2\pi} \frac{1}{2} \frac{\text{tr} \left[ \tilde{U}_\alpha^{\dagger t'}(k_y) \tau_y i \partial_{k_y} U_\alpha^{t'}(k_y) \right]}{\text{tr} \left[ \tilde{U}_\alpha^{\dagger t'}(k_y) U_\alpha^{t'}(k_y) \right]}, \end{aligned}$$

where we have inserted a normalization factor  $\text{tr} \left[ \tilde{U}_\alpha^{\dagger t}(k_x, k_y) U_\alpha^t(k_x, k_y) \right] = \text{tr} \left[ \tilde{U}_\alpha^{\dagger t}(k_y) U_\alpha^t(k_y) \right]$  to compensate for the changing norm of the state during the nonunitary evolution. Note that the same expression for  $\bar{C}_\alpha$  can be derived if the dynamics is expressed in the biorthogonal basis [112].

In previous studies, it has been shown that under the limit  $\lim_{t \rightarrow \infty} \frac{1}{t} \sum_{t'=1}^t C_x(t')$  is averaged to  $w/2$  [99] and the second line in Eq. (45) converges to  $w_\alpha/2$  [103]. Putting together, we would obtain

$$\bar{C}_\alpha = w w_\alpha / 4 = \nu_\alpha / 4 \quad (46)$$

for  $\alpha = 1, 2$  according to Eq. (26). Therefore, with the help of Eq. (27), we establish the connection between the topological invariants  $(\nu_0, \nu_\pi)$  and the MCDs as

$$\nu_0 = 2(\bar{C}_1 + \bar{C}_2) \equiv 2C_0, \quad (47)$$

$$\nu_\pi = 2(\bar{C}_1 - \bar{C}_2) \equiv 2C_\pi. \quad (48)$$

These relations have been derived before for Hermitian Floquet SOTIs [76]. Upon appropriate modifications, we find that they are also hold in non-Hermitian Floquet systems with the sublattice symmetry  $\mathcal{S}$ . Experimentally, by measuring the MCDs  $(\bar{C}_1, \bar{C}_2)$  of the dynamics over a long time-duration, we would be able to extract the topological invariants  $(\nu_0, \nu_\pi)$  for the class of non-Hermitian Floquet SOTI models studied in this work.

To be concrete, we present a typical example of the recombined MCDs  $(C_0, C_\pi)$  obtained numerically from Eq. (45) for our periodically quenched lattice model Eq. (9) in Fig. 6. The system parameters are chosen to be  $\Delta = \pi/20$ ,  $J_1 = 0.5\pi$ ,  $J_2 = 5\pi$ ,  $u = 0.25\pi$ , and the dynamics is averaged over  $M = 100$  driving periods. From Fig. 6, we see clearly that the value of  $C_0$  or  $C_\pi$  gets a quantized jump every time when the imaginary part  $v$  of the onsite potential reaches a topological phase transition point  $v_i$  ( $i = 1, \dots, 10$ ), as predicted by Eq. (31). Furthermore, between each pair of adjacent transition points, the values of  $(2C_0, 2C_\pi)$  remain quantized, equaling to the topological invariants  $(\nu_0, \nu_\pi)$  of the corresponding non-Hermitian Floquet SOTI phase as shown in Fig. 1. Putting together, we verified the correctness of the relations (47, 48) between the bulk topological invariants and MCDs of non-Hermitian Floquet SOTIs with sublattice symmetry. In the meantime, these results demonstrate the usefulness of MCDs in characterizing and detecting topological phases and phase transitions in 2D non-Hermitian Floquet systems. Numerically, we

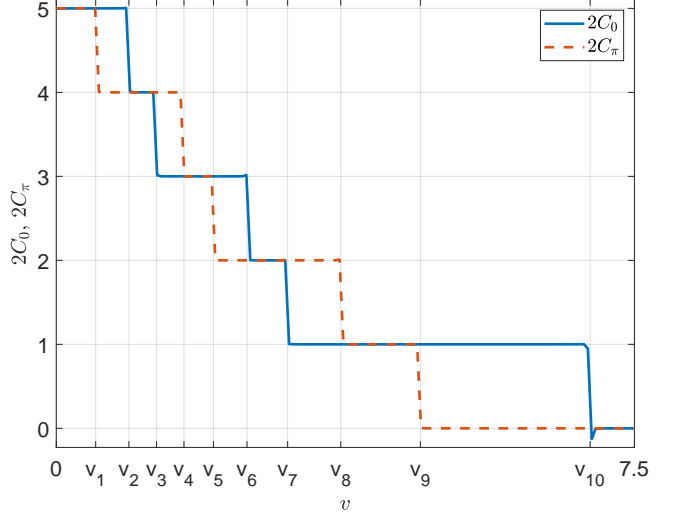


FIG. 6. The MCDs  $(C_0, C_\pi)$  versus the imaginary part of onsite potential  $v$ , after averaging over  $M = 100$  driving periods. The other system parameters are chosen as  $\Delta = \pi/20$ ,  $J_1 = 0.5\pi$ ,  $J_2 = 5\pi$  and  $u = 0.25\pi$ . The transition points  $v_i$  for  $i = 1, \dots, 10$ , separating different non-Hermitian Floquet SOTI phases, are extracted from Eq. (31). The gray horizontal grids are guiding lines of topological invariants  $(\nu_0, \nu_\pi)$  in each phase, whose values are related to the MCDs  $(C_0, C_\pi)$  through the Eqs. (47) and (48).

observe good quantizations of  $(2C_0, 2C_\pi)$  for an average over as few as  $M = 15$  driving periods, which should be well within reach under current experimental conditions.

## VII. SUMMARY

In this work, we found rich non-Hermitian Floquet SOTI phases in periodically quenched 2D lattices with balanced gain and loss. Each of the phases is characterized by a pair of integer topological invariants  $\nu_0$  and  $\nu_\pi$ , which allow us to establish the topological phase diagram of the model. We further observed multiple non-Hermitian Floquet SOTI phases with large topological invariants and various gain or loss-induced topological phase transitions. Under the OBCs, the invariants  $\nu_0$  and  $\nu_\pi$  predict the number of protected Floquet corner modes at the quasienergies zero and  $\pi$ . Thanks to the interplay between the periodic drivings and non-Hermitian effects, we found a series of non-Hermitian Floquet SOTI phases with many zero and  $\pi$  corner modes, which might be useful in quantum information technologies. Finally, we introduced a generalized version the mean chiral displacement, which could capture the topological invariants of our system through the wave packet dynamics. Our work thus extend the study of SOTIs to physical settings with both drivings, gains and losses, and unraveled the richness of non-Hermitian Floquet SOTI phases that can appear in such situations.

In future work, it would be interesting to generalize

our strategies to the engineering of non-Hermitian Floquet SOTIs in other symmetries classes and higher spatial dimensions. Moreover, in superconducting systems, the interplay between drivings and non-Hermitian effects may also induce multiple quartets of Floquet Majorana corner modes, which are potentially useful in realizing certain quantum computing tasks [77, 86].

the China Postdoctoral Science Foundation (Grant No. 2019M662444), the Fundamental Research Funds for the Central Universities (Grant No. 841912009), the Young Talents Project at Ocean University of China (Grant No. 861801013196), and the Applied Research Project of Postdoctoral Fellows in Qingdao (Grant No. 861905040009).

## ACKNOWLEDGEMENT

L.Z. is supported by the National Natural Science Foundation of China (Grant No. 11905211),

---

[1] W. A. Benalcazar, B. A. Bernevig, and T. L. Hughes, *Science* **357**, 61 (2017).  
[2] W. A. Benalcazar, B. A. Bernevig, and T. L. Hughes, *Phys. Rev. B* **96**, 245115 (2017).  
[3] Z. Song, Z. Fang, and C. Fang, *Phys. Rev. Lett.* **119**, 246402 (2017).  
[4] J. Langbehn, Y. Peng, L. Trifunovic, F. von Oppen, and P. W. Brouwer, *Phys. Rev. Lett.* **119**, 246401 (2017).  
[5] K. Hashimoto, X. Wu, and T. Kimura, *Phys. Rev. B* **95**, 165443 (2017).  
[6] F. Schindler, A. M. Cook, M. G. Vergniory, Z. Wang, S. S. P. Parkin, B. A. Bernevig, and T. Neupert, *Sci. Adv.* **4**, eaat0346 (2018).  
[7] F. Liu and K. Wakabayashi, *Phys. Rev. Lett.* **118**, 076803 (2017).  
[8] S. Franca, J. van den Brink, and I. C. Fulga, *Phys. Rev. B* **98**, 201114(R) (2018).  
[9] M. Ezawa, *Phys. Rev. Lett.* **121**, 116801 (2018).  
[10] E. Khalaf, *Phys. Rev. B* **97**, 205136 (2018).  
[11] F. Liu, H.-Y. Deng, and K. Wakabayashi, *Phys. Rev. Lett.* **122**, 086804 (2019).  
[12] L. Trifunovic and P. W. Brouwer, *Phys. Rev. X* **9**, 011012 (2019).  
[13] F. K. Kunst, G. van Miert, and E. J. Bergholtz, *Phys. Rev. B* **97**, 241405(R) (2018).  
[14] K. Kudo, T. Yoshida, and Y. Hatsugai, *Phys. Rev. Lett.* **123**, 196402 (2019).  
[15] T. I. Tuegel, V. Chua, and T. L. Hughes, *Phys. Rev. B* **100**, 115126 (2019).  
[16] F. Zangeneh-Nejad and R. Fleury, *Phys. Rev. Lett.* **123**, 053902 (2019).  
[17] O. Pozo, C. Repellin, and A. G. Grushin, *Phys. Rev. Lett.* **123**, 247401 (2019).  
[18] M. J. Park, Y. Kim, G. Y. Cho, and S. Lee, *Phys. Rev. Lett.* **123**, 216803 (2019).  
[19] Y. Hwang, J. Ahn, and B.-J. Yang, *Phys. Rev. B* **100**, 205126 (2019).  
[20] H. Araki, *Phys. Rev. Research* **2**, 012009(R) (2020).  
[21] L. Li, M. Umer, and J. Gong, *Phys. Rev. B* **98**, 205422 (2018).  
[22] R. Chen, C.-Z. Chen, J.-H. Gao, B. Zhou, and D.-H. Xu, *Phys. Rev. Lett.* **124**, 036803 (2020).  
[23] H. Li and K. Sun, *Phys. Rev. Lett.* **124**, 036401 (2020).  
[24] Y. Xu, Z. Song, Z. Wang, H. Weng, and X. Dai, *Phys. Rev. Lett.* **122**, 256402 (2019).  
[25] R. Queiroz and A. Stern, *Phys. Rev. Lett.* **123**, 036802 (2019).  
[26] R. Kozlovsky, A. Graf, D. Kochan, K. Richter, and C. Gorini, *Phys. Rev. Lett.* **124**, 126804 (2020).  
[27] R. Queiroz, I. C. Fulga, N. Avraham, H. Beidenkopf, and J. Cano, *Phys. Rev. Lett.* **123**, 266802 (2019).  
[28] Z. Yan, *Phys. Rev. Lett.* **123**, 177001 (2019).  
[29] Z. Yan, F. Song, and Z. Wang, *Phys. Rev. Lett.* **121**, 096803 (2018).  
[30] R.-X. Zhang, W. S. Cole, X. Wu, and S. Das Sarma, *Phys. Rev. Lett.* **123**, 167001 (2019).  
[31] C. Zeng, T. D. Stanescu, C. Zhang, V. W. Scarola, and S. Tewari, *Phys. Rev. Lett.* **123**, 060402 (2019).  
[32] M. Geier, L. Trifunovic, M. Hoskam, and P. W. Brouwer, *Phys. Rev. B* **97**, 205135 (2018).  
[33] X. Zhu, *Phys. Rev. Lett.* **122**, 236401 (2019).  
[34] S. A. A. Ghorashi, X. Hu, T. L. Hughes, and E. Rossi, *Phys. Rev. B* **100**, 020509(R) (2019).  
[35] D. Varjas, A. Lau, K. Pöyhönen, A. R. Akhmerov, *Phys. Rev. Lett.* **123**, 196401 (2019).  
[36] S.-B. Zhang and B. Trauzettel, *Phys. Rev. Research* **2**, 012018(R) (2020).  
[37] S. Franca, D. V. Efremov, and I. C. Fulga, *Phys. Rev. B* **100**, 075415 (2019).  
[38] Q. Wang, C.-C. Liu, Y.-M. Lu, and F. Zhang, *Phys. Rev. Lett.* **121**, 186801 (2018).  
[39] C.-H. Hsu, P. Stano, J. Klinovaja, and D. Loss, *Phys. Rev. Lett.* **121**, 196801 (2018).  
[40] Y. Volpez, D. Loss, and J. Klinovaja, *Phys. Rev. Lett.* **122**, 126402 (2019).  
[41] R.-X. Zhang, W. S. Cole, and S. Das Sarma, *Phys. Rev. Lett.* **122**, 187001 (2019).  
[42] X.-H. Pan, K.-J. Yang, L. Chen, G. Xu, C.-X. Liu, and X. Liu, *Phys. Rev. Lett.* **123**, 156801 (2019).  
[43] M. Lin and T. L. Hughes, *Phys. Rev. B* **98**, 241103(R) (2018).  
[44] D. Calugaru, V. Juricic, and B. Roy, *Phys. Rev. B* **99**, 041301(R) (2019).  
[45] B. Roy, *Phys. Rev. Research* **1**, 032048(R) (2019).  
[46] M. Ezawa, *Phys. Rev. Lett.* **120**, 026801 (2018).  
[47] B. J. Wieder, Z. Wang, J. Cano, X. Dai, L. M. Schoop, B. Bradlyn, and B. A. Bernevig, *Nat. Commun.* **11**, 627

(2020).

[48] Z. Wang, B. J. Wieder, J. Li, B. Yan, and B. A. Bernevig, Phys. Rev. Lett. **123**, 186401 (2019).

[49] E. Khalaf, H. C. Po, A. Vishwanath, and H. Watanabe, Phys. Rev. X **8**, 031070 (2018).

[50] E. Cornfeld and A. Chapman, Phys. Rev. B **99**, 075105 (2019).

[51] L. Trifunovic and P. W. Brouwer, arXiv:2003.01144.

[52] F. Schindler, Z. Wang, M. G. Vergniory, A. M. Cook, A. Murani, S. Sengupta, A. Yu. Kasumov, R. Deblock, S. Jeon, I. Drozdov, H. Bouchiat, S. Guéron, A. Yazdani, B. A. Bernevig, and T. Neupert, Nat. Phys. **14**, 918-924 (2018).

[53] S. N. Kempkes, M. R. Slot, J. J. van den Broeke, P. Capiod, W. A. Benalcazar, D. Vanmaekelbergh, D. Bercioux, I. Swart, and C. Morais Smith, Nature Materials **18**, 1292-1297 (2019).

[54] R.-X. Zhang, F. Wu, and S. Das Sarma, Phys. Rev. Lett. **124**, 136407 (2020).

[55] Y. Yang, Z. Jia, Y. Wu, Z.-H. Hang, H. Jiang, and X. C. Xie, Science Bulletin **65**, 531 (2020).

[56] X.-L. Sheng, C. Chen, H. Liu, Z. Chen, and Z.-M. Yu, Phys. Rev. Lett. **123**, 256402 (2019).

[57] M. Serra-Garcia, V. Peri, R. Süssstrunk, O. R. Bilal, T. Larsen, L. G. Villanueva, and S. D. Huber, Nature **555**, 342-345 (2018).

[58] C. W. Peterson, W. A. Benalcazar, T. L. Hughes, and G. Bahl, Nature **555**, 346-350 (2018).

[59] S. Mittal, V. V. Orre, G. Zhu, M. A. Gorlach, A. Pod-dubny, and M. Hafezi, Nature Photonics **13**, 692-696 (2019).

[60] A. E. Hassan, F. K. Kunst, A. Moritz, G. Andler, E. J. Bergholtz, and M. Bourennane, Nature Photonics **13**, 697-700 (2019).

[61] X.-D. Chen, W.-M. Deng, F.-L. Shi, F.-L. Zhao, M. Chen, and J.-W. Dong, Phys. Rev. Lett. **122**, 233902 (2019).

[62] B.-Y. Xie, G.-X. Su, H.-F. Wang, H. Su, X.-P. Shen, P. Zhan, M.-H. Lu, Z.-L. Wang, and Y.-F. Chen, Phys. Rev. Lett. **122**, 233903 (2019).

[63] Y. Ota, F. Liu, R. Katsumi, K. Watanabe, K. Wakabayashi, Y. Arakawa, and S. Iwamoto, Optica **6**, 786-789 (2019).

[64] H. Xue, Y. Yang, F. Gao, Y. Chong, and B. Zhang, Nature Materials **18**, 108-112 (2019).

[65] X. Ni, M. Weiner, A. Alù, and A. B. Khanikaev, Nature Materials **18**, 113-120 (2019).

[66] V. Peri, Z.-D. Song, M. Serra-Garcia, P. Engeler, R. Queiroz, X. Huang, W. Deng, Z. Liu, B. A. Bernevig, and S. D. Huber, Science **367**, 797-800 (2020).

[67] X. Zhang, H.-X. Wang, Z.-K. Lin, Y. Tian, B. Xie, M.-H. Lu, Y.-F. Chen, and J.-H. Jiang, Nat. Phys. **15**, 582-588 (2019).

[68] M. Weiner, X. Ni, M. Li, A. Alù, and A. B. Khanikaev, Sci. Adv. **6**, eaay4166 (2020).

[69] H. Fan, B. Xia, L. Tong, S. Zheng, and D. Yu, Phys. Rev. Lett. **122**, 204301 (2019).

[70] H. Xue, Y. Yang, G. Liu, F. Gao, Y. Chong, and B. Zhang, Phys. Rev. Lett. **122**, 244301 (2019).

[71] X. Zhang, Z.-K. Lin, H.-X. Wang, Z. Xiong, Y. Tian, M.-H. Lu, Y.-F. Chen, and J.-H. Jiang, Nat. Commun. **11**, 65 (2020).

[72] S. Imhof, C. Berger, F. Bayer, J. Brehm, L. W. Molenkamp, T. Kiessling, F. Schindler, C. H. Lee, M. Greiter, T. Neupert, and R. Thomale, Nat. Phys. **14**, 925-929 (2018).

[73] M. Serra-Garcia, R. Süssstrunk, and S. D. Huber, Phys. Rev. B **99**, 020304(R) (2019).

[74] J. Bao, D. Zou, W. Zhang, W. He, H. Sun, and X. Zhang, Phys. Rev. B **100**, 201406(R) (2019).

[75] W. Zhang, D. Zou, W. He, J. Bao, Q. Pei, H. Sun, and X. Zhang, arXiv:2001.07931.

[76] R. W. Bomantara, L. Zhou, J. Pan, and J. Gong, Phys. Rev. B **99**, 045441 (2019).

[77] R. W. Bomantara and J. Gong, Phys. Rev. B **101**, 085401 (2020).

[78] Y. Peng and G. Refael, Phys. Rev. Lett. **123**, 016806 (2019).

[79] H. Hu, B. Huang, E. Zhao, and W. V. Liu, Phys. Rev. Lett. **124**, 057001 (2020).

[80] T. Nag, V. Juricic, and B. Roy, Phys. Rev. Research **1**, 032045(R) (2019).

[81] M. Rodriguez-Vega, A. Kumar, and B. Seradjeh, Phys. Rev. B **100**, 085138 (2019).

[82] R. Seshadri, A. Dutta, and D. Sen, Phys. Rev. B **100**, 115403 (2019).

[83] K. Plekhanov, M. Thakurathi, D. Loss, and J. Klinovaja, Phys. Rev. Research **1**, 032013(R) (2019).

[84] Y. Peng, Phys. Rev. Research **2**, 013124 (2020).

[85] A. K. Ghosh, G. C. Paul, and A. Saha, arXiv:1911.09361.

[86] R. W. Bomantara, arXiv:2003.05181.

[87] T. Liu, Y.-R. Zhang, Q. Ai, Z. Gong, K. Kawabata, M. Ueda, and F. Nori, Phys. Rev. Lett. **122**, 076801 (2019).

[88] Z. Zhang, M. R. López, Y. Cheng, X. Liu, and J. Christensen, Phys. Rev. Lett. **122**, 195501 (2019).

[89] X.-W. Luo and C. Zhang, Phys. Rev. Lett. **123**, 073601 (2019).

[90] C. H. Lee, L. Li, and J. Gong, Phys. Rev. Lett. **123**, 016805 (2019).

[91] M. Ezawa, Phys. Rev. B **99**, 201411(R) (2019).

[92] M. Ezawa, Phys. Rev. B **99**, 121411(R) (2019).

[93] E. Edvardsson, F. K. Kunst, and E. J. Bergholtz, Phys. Rev. B **99**, 081302(R) (2019).

[94] A. Yoshida, Y. Otaki, R. Otaki, and T. Fukui, Phys. Rev. B **100**, 125125 (2019).

[95] J. K. Asbóth, L. Oroszlány, and A. Pályi, *A Short Course on Topological Insulators* (Springer, Switzerland, 2016).

[96] J. K. Asbóth, Phys. Rev. B **86**, 195414 (2012). J. K. Asbóth, and H. Obuse, Phys. Rev. B **88**, 121406 (2013).

[97] F. Harper, R. Roy, M. S. Rudner, and S. L. Sondhi, Annu. Rev. Condens. Matter Phys. **11**, 345-368 (2020).

[98] D. Y.H. Ho and J. Gong, Phys. Rev. B **90**, 195419 (2014).

[99] L. Zhou and J. Gong, Phys. Rev. A **97**, 063603 (2018).

[100] K. Yang, L. Zhou, W. Ma, X. Kong, P. Wang, X. Qin, X. Rong, Y. Wang, F. Shi, J. Gong, and J. Du, Phys. Rev. B **100**, 085308 (2019).

[101] L. Zhou and Q. Du, Phys. Rev. A **101**, 033607 (2020).

[102] L. Zhou and J. Gong, Phys. Rev. B **98**, 205417 (2018).

[103] L. Zhou and J. Pan, Phys. Rev. A **100**, 053608 (2019).

[104] L. Zhou, Phys. Rev. B **100**, 184314 (2019).

[105] L. Zhou, Phys. Rev. B **101**, 014306 (2020).

[106] F. Cardano, A. D'Errico, A. Dauphin, M. Maffei, B. Piccirillo, C. de Lisio, G. D. Filippis, V. Cataudella, E. Santamato, L. Marrucci, M. Lewenstein and P. Massignani, Nat. Commun. **8**, 15516 (2017).

- [107] M. Maffei, A. Dauphin, F. Cardano, M. Lewenstein and P. Massignan, *New J. Phys.* **20**, 013023 (2018).
- [108] A. D'Errico, F. D. Colandrea, R. Barboza, A. Dauphin, M. Lewenstein, P. Massignan, L. Marrucci, and F. Cardano, arXiv:2001.05960.
- [109] E. J. Meier, F. A. An, A. Dauphin, M. Maffei, P. Massignan, T. L. Hughes, and B. Gadway, *Science* **362**, 929 (2018).
- [110] D. Xie, T.-S. Deng, T. Xiao, W. Gou, T. Chen, W. Yi, and B. Yan, *Rhys. Rev. Lett.* **124**, 050502 (2020).
- [111] The formula  $\text{tr}(A \otimes B) = \text{tr}(A)\text{tr}(B)$  for the tensor product of operators  $A$  and  $B$  has been used to arrive at this relation.
- [112] D. C. Brody, *J. Phys. A: Math. Theor.* **47**, 035305 (2014).